https://doi.org/10.1016/j.jallcom.2020.157218
This is the Pre-Published Version.

Quantitative investigation on deep hydrogen trapping in tempered martensitic steel

Rongjian Shi [a, b], Lin Chen [a, b], Zidong Wang [c], Xu-Sheng Yang [d], Lijie Qiao [a, b, *], Xiaolu Pang [a, c, *]

[a] *Beijing Advanced Innovation Center for Materials Genome Engineering, University of Science and Technology Beijing, Beijing 100083, China*

[b] *Corrosion and Protection Center, University of Science and Technology Beijing, Beijing 100083, China*

[c] *School of Materials Science and Engineering, University of Science and Technology Beijing, Beijing 100083, China*

[d] *Advanced Manufacturing Technology Research Centre, Department of Industrial and Systems Engineering, The Hong Kong Polytechnic University, Hung Hom, Kowloon, Hong Kong, China*

* Corresponding authors.

Email addresses: lqiao@ustb.edu.cn (L. Qiao), pangxl@mater.ustb.edu.cn (X. Pang).

Abstract

In this work, the correlation between different microstructural components and hydrogen trapping with high density in tempered niobium carbide (NbC)-precipitated martensitic steel was quantitatively investigated using a combination of electrochemical hydrogen permeation experiments and thermal desorption spectroscopy. The martensite lath and a high density of dislocations, which constitute the reversible hydrogen trapping sites, with a density of 2.24×10^{20} cm^{-3} in Fe-0.05C-1.10Mn-4.50Ni-0.50Cr-0.50Mo-0.05Nb wt.% martensitic steel. The dislocation with high density could disperse the hydrogen distribution. Furthermore, the uniformly distributed NbC nanoprecipitates, the high-angle grain boundaries, and the grain-boundary precipitates were

© 2020. This manuscript version is made available under the CC-BY-NC-ND 4.0 license http://creativecommons.org/licenses/by-nc-nd/4.0/

found to act as irreversible hydrogen traps, with a density of 1.00×10^{20} cm^{-3}. These deep hydrogen trapping sites could not only trap hydrogen irreversibly, but also can inhibit the accumulation of hydrogen. The interpretation of hydrogen trapping is significant to enhance the hydrogen embrittlement resistance of high-strength martensitic steels.

Keywords: Hydrogen embrittlement; Martensitic steels; Hydrogen traps; Precipitation; Transmission electron microscopy.

1. Introduction

High-strength tempered martensitic steels exhibit excellent mechanical properties because of their high strength and ductility, which enables them to meet modern industrial requirements such as those encountered in oil and gas exploitation and marine engineering [1-3]. However, the hydrogen embrittlement (HE) sensitivity of these steels increases dramatically with increasing mechanical strength [4, 5]. The hydrogen-enhanced decohesion (HEDE) mechanism [6] results in a reduction in the cohesive bond energy among atoms in the presence of hydrogen. The high-strength steels generally display brittle fracture mode, such as intergranular failure, with the accumulation of hydrogen, especially fractured in the elastic range [7-9]. Thus, the design of hydrogen trapping sites in the interior of the grains, instead of distributing along grain boundaries, are urgently needed to suppress catastrophic intergranular failure.

Hydrogen traps have the potential to provide HE resistance, and quantifying the hydrogen concentration and trapping sites in steels is critical [10, 11]. Hydrogen traps can be divided into reversible and irreversible hydrogen traps according to the hydrogen binding energy. Reversible traps (e.g., lath boundaries [12] and dislocations [13]) are characterized by a low binding energy with hydrogen ($15 \leq E_b \leq 35$ kJ/mol). Hydrogen trapped by the reversible traps can escape from the trapping sites at room temperature, and hydrogen accumulates in local regions because of high stress or strain, thus inducing fracture [14]. Irreversible traps (e.g., precipitates [15, 16] and

high-angle grain boundaries [17]), where the E_b is high ($40 \leq E_b \leq 100$ kJ/mol), are considered to impede the movement of hydrogen and improve the HE resistance [10, 18]. However, the accumulation of hydrogen at grain boundaries in martensitic steels could induce the intergranular failure in the stress-strain behavior, resulting in premature fracture [9]. It's vital for improving the HE resistance that the deep hydrogen trapping sites with high density inside the grain are designed to disperse the hydrogen distribution [8]. In the case of martensitic steels, the density of hydrogen trapping sites is typically 10^{17}-10^{20} cm^{-3} [19-21]. Indeed, the complex microstructures of martensitic steels make characterization of the different hydrogen trapping abilities difficult; consequently, the interactions between hydrogen and various microstructures have not yet been fully elucidated [19].

Several analytical techniques, such as electrochemical hydrogen permeation or thermal desorption spectroscopy (TDS), can be used to characterize hydrogen traps [2, 10, 19, 22-25]. Furthermore, the hydrogen permeability and hydrogen trapping abilities were widely performed to determine HE in martensitic high-strength steels [26-28]. However, a synergistic evaluation of the correlation between different microstructural components and hydrogen trapping is still lacked to be investigated quantitatively until now. In combination with the characteristics of various microstructures with specific binding energies, the hydrogen concentration and the density of hydrogen traps can provide valuable information for understanding the hydrogen trapping phenomenon [29, 30]. Therefore, an appropriate design that increases the density of hydrogen trapping sites offers much more potential for controlling the distribution of hydrogen and guiding the further optimization of HE resistance.

In the present work, the density of hydrogen trapping sites and hydrogen trapping capacity of different microstructures in tempered martensitic steel were investigated by using a combination of electrochemical hydrogen permeation, TDS, and various microstructure observations. The results provide systematic experimental evidence revealing the correlation between different microstructural components and deep hydrogen trapping with high density in tempered martensitic steel with niobium

carbide (NbC) precipitates.

2. Material and methods

2.1 Materials and heat treatment

The test material in this study was NbC-precipitation-strengthened martensitic steel. The chemical composition of the investigated steel was based on the HSLA-100 steel with Fe-0.05C-1.10Mn-4.50Ni-0.50Cr-0.50Mo-0.05Nb wt.%. The as-received rolled plates were 10 mm in thickness and were subsequently cut into blocks with 50 mm long (rolling direction), 30 mm wide, and 10 mm thick by electro discharge machining (EDM). The quenching and tempering heat treatment was then performed to obtain the investigated tempered martensitic steel. The as-rolled samples were solution treated at 1200 ˚C for 10 min, followed by water quenching. The quenched steels were subsequently tempered at 500 ˚C for 1 h and then air cooled to room temperature.

2.2 X-ray diffraction (XRD) analysis

Quantitative XRD analysis was performed on a TTR Ⅲ X-ray diffractometer at room temperature. Before X-ray analysis, the specimens were electrochemically polished in the solution of 5 vol% perchloric acid and 95 vol% ethanol with a voltage of 30 V for 15 seconds to relieve deformed zones on the surfaces. The XRD analysis was performed with Cu Kα radiation (wavelength, $\lambda = 0.1542$ nm), with normal focus tubes (40 kV, 30 mA). The diffraction patterns were recorded from $2\theta = 40$ to 120° with a step of 0.01° and 15 s/step to cover the diffractions of (110), (200), (211), (220) and (310) lattice planes.

2.3 Microstructure characterization

Specimens were mechanically polished and then etched with 4% nital solution for microstructural examination using a Zeiss Supra55 scanning electron microscope.

Furthermore, the microstructure and distribution of NbC nanoprecipitates and the atomic arrangement of the interfaces between the nanoparticles and the matrix were characterized in detail by high-resolution transmission electron microscopy (HRTEM) using an instrument (JEOL JEM-2100) operated at an accelerating voltage of 200 kV. The foil samples for TEM observation were prepared by twin-jet electropolishing in an electrolyte composed of 10 vol.% $HClO_4$ in methanol electrolyte at a low temperature (−30 ˚C) and with a direct current (DC) potential of 30 V.

2.4 Electrochemical hydrogen permeation tests

Electrochemical hydrogen permeation tests were conducted in a modified Devanathan-Stachurski cell with anodic and cathodic compartments [31]. To eliminate the influence of surface adsorption, the specimen thickness was 1.2 mm [32] and the area of the tested region in contact with the solution was 0.785 cm^2 (with a diameter of 10 mm). Prior to electrochemical permeation tests, specimens with dimensions of 20 mm × 20 mm × 1.3 mm cut through EDM were polished using SiC papers to 5000 grit progressively and then were polished with 40 nm silicon dioxide suspension to avoid surface residual strain; the final thickness of the specimen was 1.2 mm. To protect the specimens against anodic dissolution, the ~100 nm nickel film was sputtered with Magnetron Sputtering Film Deposition System (LAB 18) on the exit side of all of the specimens. The electrolyte of the charging cell composed of 0.2 mol/ L sodium hydroxide (NaOH) with 0.22 g/L thiourea, and that of the detection cell was 0.2 mol/L NaOH. The anodic compartment was controlled by an electrochemical workstation (Ivium-n-Stat), which provided a potential of 280 mV; the cathodic compartment was controlled by a DC source (ITECH 6133B) with a current density of 2 mA/cm^2. A saturated calomel electrode was used as a reference electrode in the anodic compartment, and platinum wire was used as counter electrodes in both compartments. A two-step polarization procedure was applied to determine the density of the reversible and irreversible hydrogen traps in the specimens. After the first polarization reached a steady state, the cathodic hydrogen charging was stopped.

The second permeation transient was then started after the current in the first polarization discharge reached the background current. The first and second permeation transients were based on the same hydrogen charging condition to eliminate the effects of the formed oxide [33].

2.5 Thermal desorption spectroscopy (TDS) analysis

TDS analysis was conducted to identify the capacity of hydrogen trapping sites [34]. Specimens for TDS analysis with dimensions of 30 mm (rolling direction) × 10 mm × 1.6 mm cut through EDM were polished using SiC papers to 5000 grit progressively and then cleaned ultrasonically in acetone. To determine the hydrogen content, specimens with final dimensions of 30 mm × 10 mm × 1.5 mm were electrochemically charged in 0.2 mol/L NaOH at a current density of 2 mA/cm^2. The applied TDS apparatus is the commercial HTDS-002 supplied by R-DEC Co., Ltd; the measurement accuracy was estimated for ±0.01 ppm. The hydrogen pre-charged specimens were immediately immersed into liquid nitrogen before analysis by TDS. The equipment has been vacuumized before the test. The specimens were also cleaned with ethanol and air-dried before TDS analysis (within 5 min). Hydrogen determination by TDS was carried out via quadrupole mass spectrometry with the heating rate of 100 ˚C/h, immediately after the vacuum level was sufficiently low (~10^{-11} Pa).

3. Results

3.1 Microstructure characterization

The XRD pattern of the investigated quenched and tempered steel shown in Fig. 1(a) indicates that there is single body centered cubic (bcc) crystal structure, without any retained austenite. Fig. 1(b, c) shows the microstructure of quenched and tempered steel specimens, as observed by scanning electron microscopy (SEM). The red and yellow dashed lines indicate the grain boundaries and lath boundaries,

respectively. A high density of typical tempered lath martensite is observed to be distributed homogeneously. The orientation of the lath martensite varies substantially in different prior austenite grains, as indicated in the corresponding enlarged view in the inset of Fig. 1(c).

3.2 Evaluation of hydrogen permeation and density of hydrogen trapping sites

The hydrogen diffusion and permeation behavior in the investigated steel was characterized on the basis of the hydrogen permeation curve, which is presented in Fig. 2(a). To determine both the reversible and irreversible hydrogen traps, a secondary permeation cycle was conducted; the results are presented in Fig. 2(b). The hydrogen permeation curves indicate an initial increase in the current density, followed by a steady state. The density of total hydrogen trapping sites, including all reversible and irreversible hydrogen traps, was obtained from the first permeation test. The density of reversible trapping sites was then obtained from the second permeation test because the irreversible traps were filled in the first permeation test, and none of them participated in the second permeation [24].

The electrochemical hydrogen permeation parameters, including the saturated current density (I_∞/A), the time lag for 0.63 saturation ($t_{0.63}$), hydrogen permeability ($J_\infty L$), effective hydrogen diffusion coefficient (D_{eff}), apparent hydrogen solubility (C_{ap}), and the density of hydrogen trapping sites (N_t) were obtained from permeation curves and the following equations [22, 23, 31]:

$$J_\infty L = I_\infty L / FA \tag{1}$$

$$D_{\text{eff}} = L^2 / 6t_{0.63} \tag{2}$$

$$C_{\text{ap}} = J_\infty L / D_{\text{eff}} \tag{3}$$

$$N_t = C_{\text{ap}} \left(D_{\text{l}} / D_{\text{eff}} - 1 \right) / 3 \tag{4}$$

$$N_{ir} = N_{t1} - N_{t2} \tag{5}$$

where I_∞(μA), L (cm), F (C/mol), and A (cm^2) are the saturated current, thickness of the specimen, Faraday constant (96,500 C/mol), and test area exposed in the charging

and detection cells, respectively. D_1 is the value of the lattice diffusion coefficient in pure trap-free bcc iron ($D_1 = 1.28 \times 10^{-4}$ cm^{2}s^{-1}) [22]. N_{ir}, N_{t1}, and N_{t2} are the density of irreversible hydrogen traps and the densities of hydrogen traps in the first and second permeation, respectively. In addition, the density of hydrogen traps in the second permeation was equivalent to the density of reversible hydrogen traps ($N_r = N_{t2}$).

The results of the hydrogen permeation parameters and the density of hydrogen trapping sites are listed in Table 1. To verify the accuracy of the proposed hydrogen diffusion coefficient, the hydrogen permeation transient (rise transient) can be fitted in the following equation [33]:

$$\frac{i_t - i_0}{i_\infty - i_0} = \frac{2L}{\sqrt{\pi D_{\text{eff}} t}} \sum_{n=0}^{\infty} \exp\left[-\frac{(2n+1)^2 L^2}{4 D_{\text{eff}} t} \right] \quad (6)$$

where i_t, i_0, i_∞ are the permeation current density at t, the initial steady permeation current density at t=0, and the steady permeation current density at $t \to \infty$, respectively. As shown in Fig. 2, the experimental results were well fitted by the theoretical curves (dotted curves), which were determined by the D_{eff} in Table 1.

The hydrogen permeation results provide important information about the hydrogen diffusion and trapping behaviors. The effective hydrogen diffusion coefficient increases and the apparent hydrogen solubility decreases in the second permeation curve because deep hydrogen traps are fully filled during the first hydrogen permeation. Meanwhile, the density of reversible hydrogen trapping sites ($N_r = N_{t2}$) is 2.24×10^{20} cm^{-3}, and the density of irreversible hydrogen trapping sites ($N_{ir} = N_{t1} - N_{t2}$) is 1.00×10^{20} cm^{-3}. Notably, the N_r is approximately twice as large as the N_{ir}. Dislocations, lath boundaries, grain boundaries, and precipitates strongly influence the permeability and solubility of hydrogen [35], which will be discussed in the following section.

3.3 TDS results and estimation of the hydrogen trapping capacity

The hydrogen concentration distribution could be almost homogeneous assuming

that the concentration of hydrogen at the surface is a constant and homogenization can be achieved when the center of the sample reaches the saturation state before TDS. The hydrogen concentration at the mid-plane of the plate is given by the following equation [36]:

$$C_{L/2} = C_0 \left[1 - \frac{4}{\pi} \sum_{n=0}^{\infty} \frac{1}{2n+1} \exp\left\{ -\frac{D_{\text{eff}} (2n+1)^2 \pi^2 t_c}{L^2} \right\} \right] \quad (7)$$

where $C_{L/2}$, C_0, t_c, and L are the hydrogen concentration at the mid-plane of the plate, the constant concentration of hydrogen at the surface of the sample, the hydrogen charging duration, and the thickness of the sample, respectively. In the present work, L = 1.5 mm, D_{eff} = 1.63×10^{-6} cm^2/s. The relationship between hydrogen charging time and the hydrogen concentration at the mid-plane of the plate is shown in Fig. 3(a). The time required for 1.5 mm-thick TDS specimens to be filled with hydrogen to saturation is calculated to be 3 h (10800 s). Given the complexity of the microstructure, the specimens were charged for 10 h to ensure hydrogen saturation [13].

The TDS results for the investigated steel are shown in Fig. 3(b); three peaks are observed in the hydrogen desorption rate curve. The first peak (145 ˚C corresponds to the reversible traps, which other authors have attributed to martensitic lath boundaries, grain boundaries, and high-density dislocations with activation energies of 15 to 35 kJ/mol [37, 38]. Also, the second (290 ˚C) and third (350 ˚C) peak are generated by desorption of hydrogen from irreversible traps with an activation energy greater than 40 kJ/mol [39]. The hydrogen concentration trapped by different microstructures, C_H, can be derived with the equation [40]

$$C_H = Q \int_0^{t_m} (p - p_b) \mathrm{d}t \Big/ RT \quad (8)$$

where Q, R, T, t, t_m, p, and p_b are the effective pumping speed, which was notionally constant, the gas constant, the absolute temperature, the pumping time, the time of measurement, the measured hydrogen pressure, and the background pressure, respectively. The value of the integral was obtained from the area under the curve of

the hydrogen desorption rate versus time. With respect to the determination of the hydrogen trapping capacity, the reversible ($15 \leq E_b \leq 35$ kJ/mol) hydrogen content was 0.82 $\pm$ 0.03 ppm (by weight), whereas the irreversible ($40 \leq E_b \leq 100$ kJ/mol) hydrogen content was 0.38 $\pm$ 0.02 ppm (by weight). The reversible hydrogen content was approximately twice the irreversible hydrogen content at the specific hydrogen charging condition in the present study, consistent with the hydrogen trap ratio calculated on the basis of the hydrogen permeation results. It should be pointed out that the trapped hydrogen content is a variable value with different hydrogen charging conditions, and the ration of hydrogen distributed to the irreversible hydrogen trapping sites would be increased when decreasing the hydrogen charging current density [41-43].

4. Discussion

4.1 Reversible hydrogen trapping of martensitic lath boundary and dislocations

Hydrogen permeation and trapping capacity should be discussed separately for different hierarchies of microstructures [16, 44] (i.e., high-angle grain boundaries, lath boundaries, dislocations, and precipitates) because of the complexity of the martensitic structure.

The lath boundary is a low-angle grain boundary composed of edge and screw dislocations, with a hydrogen binding energy of 15-35 kJ/mol [12, 45, 46]. TEM images showing the microstructure of the martensite lath distribution are presented in Fig. 4(a)-(b). A high density of martensite lath is observed (see Fig. 1 for details of the SEM micrograph), with a mean lath width of a few hundred nanometers, as marked by the yellow dashed lines. Dislocations play a critical role in hydrogen permeation and trapping in steels [13, 47]. Fig. 4(c) and (d) shows TEM images indicating the distribution of dislocations and the interaction between dislocations and nanoprecipitates (dislocations and nanoprecipitates are indicated by arrows and arrowheads, respectively). Uniformly distributed dislocation lines are also observed,

along with a high density of dislocation pile-ups.

The average dislocation density, ρ, can be measured by XRD of the investigated steel. The XRD patterns of the investigated steels in Fig. 1(a) indicate that they are composed entirely of tempered martensite. The full-width at half-maximum was analyzed among five XRD peaks, (110), (200), (211), (220), and (310) planes, which are shown in Fig. 5(a)-(e). The XRD peak width is related to the strain through the Williamson-Hall (WH) equation [48]:

$$\delta_{hkl}\cos\theta_{hkl}/\lambda = 1/D + 4e\sin\theta_{hkl}/\lambda \quad (9)$$

where θ_{hkl}, λ, e, and D are the diffraction angle at the selected peak position, X-ray wavelength, effective mean microstrain, and the mean size of the coherently diffracting domains, respectively. In addition, δ_{hkl} is measured on a scale of $2\theta_{hkl}$. The dislocation density, ρ, is then calculated by the following equation [49]:

$$\rho = 14.4e^2/b^2 \quad (10)$$

where b is the Burger's vector (b = 0.25 nm). The variation of the diffraction peaks corresponding to the (110), (200), (211), (220), and (310) planes is shown in Fig. 5 (a), (b), (c), (d), and (e), respectively. Plotting $\delta_{hkl}\cos\theta_{hkl}/\lambda$ vs. $4\sin\theta_{hkl}/\lambda$ should generate a straight line with a slope providing a value for e. The WH plots for the tempered specimen are shown in Fig. 5(f). The dislocation density was calculated to be (3.4 ± 0.3) $\times 10^{10}$ cm^{-2}.

Dislocations are considered to be reversible traps because of their low binding energy ($20 \leq E_b \leq 35$ kJ/mol) [17, 50-52]. The dislocation density is generally 10^9-10^{10} cm^{-2} in in ferritic or martensitic steel [13, 17] so that the dislocation with high density (3.4×10^{10} cm^{-2}) in this study could trap plenty of hydrogen. According to the HELP mechanism [53], hydrogen leads to localized plastic deformation due to dislocation shielding. Moreover, according to the adsorption-induced dislocation emission mechanism [54], hydrogen enhances dislocations nucleation, leading to premature fracture. Furthermore, the hydrogen concentration in the susceptible region can be enriched by mobile dislocations. Thus, the cohesive bond energy among the atoms can be reduced in the presence of hydrogen (i.e., HEDE [6]). Therefore,

altering the dislocation configurations and density could represent a reasonable approach to optimizing HE in steels.

4.2 Irreversible hydrogen trapping of NbC nanoprecipitates and high-angle grain boundaries

Numerous investigations designed to reveal the location of the hydrogen trapping sites in various carbides have been reported. For NaCl-type alloy carbides, various calculations (with various assumptions) and experiments related to the hydrogen trapping sites in carbide nanoprecipitates at room temperature have been conducted, including calculations and experiments related to the core of misfit dislocations on a semi-coherent interface [18, 55-58], carbon vacancies on a (001) coherent interface of carbide precipitates [59], carbon vacancies within the core of carbides [60, 61], and incoherent interfaces [8].

In the present study, Fig. 6(a) presents the TEM image of the microstructure and distribution of the precipitates in the in the investigated tempered martensitic steel, where Fig. 6(b) indicates the corresponding enlarged view of the dotted box. In addition, Fig. 6(c) and (d) shows a bright-field TEM image, where the inset is the corresponding selected-area diffraction pattern (SADP), and a dark-field TEM image of the nanoprecipitates, respectively. Numerous precipitates with a mean size of 9 nm are uniformly dispersed in the Fe matrix. The carbide size distribution is shown in Fig. 6(e), and the average diameter of NbC nanoprecipitates is 9.3 ± 2.2 nm by calculating more than 200 nanoprecipitates. However, according to the previous literature, the NbC just grows to within 5 nm in diameter during tempering in a similar Nb-bearing tempered martensitic steel [62, 63], which is much smaller than that in this work; this will be explained in the following. With the uniformly dispersed NbC precipitates in this study, a great amount of hydrogen can be trapped irreversibly, which is important to designing embrittlement-resistant steels [8].

The HRTEM observation of one NbC with the dimeter of approximately 12 nm along $[11\bar{0}]_{NbC} // [001]_{\alpha\text{-Fe}}$ direction is shown in Fig. 7. Fig. 7(a) shows the HRTEM

image of the NbC with the surrounding martensite matrix. Fig. 7(b1-b2) are respectively fast Fourier transformation (FFT) and inversed FFT (IFFT) taken from the selected yellow box in (a), showing the fcc NbC along [110] zone axis. The atomic spacing of 2.60 Å indicates the $(111)_{NbC}$ planar spacing. Fig. 7(b3-b4) are respectively FFT and IFFT taken from the selected red box in (a), showing the bcc α-Fe matrix along [001] zone axis. The atomic spacing of 2.03 Å indicates the $(110)_{\alpha\text{-Fe}}$ crystallographic planar spacing. Fig. 7(c) presents the corresponding FFT patterns of the NbC with the surrounding matrix. Besides, the IFFT image of the NbC and the surrounding matrix is shown in Fig. 7(d); Fig. 7(e) presents the enlarged image in dashed rectangle in (d) showing the interfacial structures for the NbC/-Fe interface. The diffraction spots are schematically summarized in Fig. 7(f), showing no obvious orientation relationship (OR) observed; this is neither the traditional Baker-Nutting (B-N) OR [64], with $(001)_{Carbide}$ // $(010)_{\alpha\text{-Fe}}$ and $[11\ 0]_{Carbide}$ // $[001]_{\alpha\text{-Fe}}$, nor the Nishiyama-Wassermann (N-W) OR [65], with $(111)_{Carbide}$ // $(110)_{\alpha\text{-Fe}}$ and $[11\ 0]_{Carbide}$ // $[001]_{\alpha\text{-Fe}}$. Moreover, the OR between NbC precipitate and martensite matrix might be the incoherent OR, which can trap hydrogen stably. This result is consistent with a previously reported direct observation that hydrogen atoms locate at the interfaces between NbC precipitates and the matrix [8]. Therefore, the nanoscale NbC precipitates, which act as the irreversible hydrogen trapping sites, exhibit a high-temperature peak in TDS, with a high binding energy ($40 \leq E_b \leq 100$ kJ/mol) [39, 45, 66-70].

In addition, the prior austenite grain boundary is a kind of high-angle grain boundary, as indicated in Fig. 1(b, c), which can impede the dislocation movement, leading to the dislocation accumulation at grain boundaries. The high-angle grain boundary, with a binding energy of $40 \leq E_b \leq 60$ kJ/mol [17, 71], can play a critical role in HE [72-75]. Besides, the interfaces between the grain-boundary precipitates and matrix are effective hydrogen trapping sites [76, 77]. The presence of grain boundaries and grain-boundary precipitates in the present study, along with the

diffraction spots and the corresponding EDS spectra, is shown in Fig. 8. Fig. 8(a, b) shows typical TEM bright-field micrographs of grain boundaries with grain-boundary precipitates. Fig. 8(c, d) and (e) show the SADP and the corresponding EDS spectra of the white dashed circle in (b), respectively. The corresponding diffraction spots of SADP in Fig. 8(c), as listed in Table 2, indicate three sets of spots. The atomic planar spacing and the inclined angles measured from SADP, which well fit the calculation results [78], indicate that there are two α-Fe grains and one NbC grain-boundary precipitate. The EDS results indicate that their compositions include Fe, C, Ni, and Nb, as shown in Fig. 8(e). These grain-boundary precipitates are confirmed as NbC precipitates through the combination of SADP and EDS analyses. These grain boundaries and grain-boundary precipitates could also be irreversible hydrogen trapping sites.

To reveal the reason for generating incoherent NbC, which can be irreversible hydrogen trapping sites, in the tempered martensitic steels, further microstructural investigation on as-quenched specimen was also performed. There are many fine undissolved nanoparticles, which might have not been fully dissolved and retained after solution treatment [79], as indicated by the arrows in Fig. 9(a-b). This could be due to the short duration of the solution treatment (1200 ˚C for 10 min) [80]. In addition, Fig. 9(c) presents the EDS spectra and the element contents shown by the red dashed circle in Fig. 9(b), indicating the large undissolved nanoparticle is NbC. Moreover, the OR between NbC precipitate (~12 nm) and martensite matrix might be the incoherent OR. Thus, these incoherent NbC observed in the tempered martensitic steels in this study may be inherited from the undissolved NbC precipitate that may be retained after solution treatment, which still needs further investigations in the future.

In summary, the different hydrogen trapping capacity is manifested by the different microstructures in tempered martensitic steel. Fig. 10 shows a schematic of the hydrogen trapping of different microstructures in tempered martensitic steel. Three hydrogen trapping models are proposed in this study. In model (I), the martensite lath and dislocations with high density constitute the reversible hydrogen trapping sites with the density of 2.24×10^{20} cm^{-3}, which can trap 0.82 ppm (3.90 ×

10^{18} atoms/cm^3) hydrogen at the specific hydrogen charging condition in the present study. In models (II) and (III), the uniformly distributed NbC precipitates, the high-angle grain boundaries, and the grain-boundary precipitates can act as irreversible hydrogen trapping sites, with a density of 1.00×10^{20} cm^{-3}, which can trap 0.38 ppm (1.81×10^{18} atoms/cm^3) hydrogen in this study. Compared with the densities of various hydrogen trapping sites from hydrogen permeation tests, the amounts of trapped hydrogen obtained by TDS analysis are much lower. One possible reason for this difference is the assigned value of the lattice diffusion coefficient in trap-free bcc iron, D_l, because N_t is proportional to D_l according to Eq. (5). There are also many different D_l in the literature based on experimental results, such as 1.29×10^{-6} cm^{2}s^{-1} in 3.5NiCrMoV steel [81], 2.07×10^{-6} cm^{2}s^{-1} in 980DP steel [21], and 7.20×10^{-5} cm^{2}s^{-1} in X70 pipeline steel [82]. The density of hydrogen trapping sites would be similar in magnitude with hydrogen concentration by using the aforementioned D_l. Thus, it is important to obtain the hydrogen lattice diffusivity with increasing hydrogen input fugacity [21, 81] in further investigation. However, in this study, the relative magnitude between reversible and irreversible hydrogen amounts in TDS is consistent with the amounts of hydrogen trapping sites in hydrogen permeation. Furthermore, from the microstructure perspective, the dislocation with high density (3.4×10^{10} cm^{-2}) in this study could trap plenty of hydrogen as reversible hydrogen trapping sites to disperse the hydrogen distribution, especially. On the other hand, the deep hydrogen trapping sites have great potential for improving the HE resistance by uniform distribution of hydrogen. They could not only trap hydrogen irreversibly, but also impede dislocation motion through dislocation-particle interaction during plastic deformation [83, 84], which can inhibit the accumulation of hydrogen. These complex microstructures are responsible for the deep hydrogen trapping of tempered martensitic steel. The quantitative evaluation of the correlation between different microstructural components and deep hydrogen trapping with high density in tempered martensitic steel is important for enhancing the HE resistance [85].

5. Conclusions

The density of the hydrogen trapping sites and the hydrogen trapping capacity of different microstructures in tempered martensitic steel were investigated using a combination of electrochemical hydrogen permeation measurements, TDS, and SEM and TEM observations.

(1) The martensite lath and dislocations with notably high density constitute the reversible hydrogen trapping sites, with the density of 2.24×10^{20} cm^{-3}. The dislocation with high density (3.4×10^{10} cm^{-2}) could trap plenty of hydrogen to disperse the hydrogen distribution, particularly.

(2) The uniformly distributed NbC precipitates, the high-angle grain boundaries, and the grain-boundary precipitates act as irreversible hydrogen trapping sites, with the density of 1.00×10^{20} cm^{-3}. These deep hydrogen trapping sites could not only trap hydrogen irreversibly, but also impede dislocation motion during plastic deformation, which can inhibit the accumulation of hydrogen.

Declaration of competing interest

The authors declare that they have no known competing financial interests or personal relationships that could have appeared to influence the work reported in this paper.

CRediT authorship contribution statement

Rongjian Shi: Investigation, Methodology, Validation, Writing - original draft. **Lin Chen:** Writing - review & editing. **Zidong Wang:** Conceptualization, Validation. **Xu-Sheng Yang:** Validation, Writing - review & editing. **Lijie Qiao:** Validation, Writing - review & editing, Supervision. **Xiaolu Pang:** Validation, Writing - review & editing, Supervision.

Acknowledgments

This work was supported by the National Natural Science Foundation of China (No. U1706221, 51922002, 51771025). The author R. Shi would like to acknowledge the especial sponsor for the Research Student Attachment Programme from the graduate school of University of Science and Technology Beijing.

References:

[1] J. Lee, T. Lee, Y.J. Kwon, D.J. Mun, J.Y. Yoo, C.S. Lee, Effects of vanadium carbides on hydrogen embrittlement of tempered martensitic steel, Met. Mater. Int. 22 (2016) 364-372. https://doi.org/10.1007/s12540-016-5631-7.

[2] S. Zhang, E. Fan, J. Wan, J. Liu, Y. Huang, X. Li, Effect of Nb on the hydrogen-induced cracking of high-strength low-alloy steel, Corros. Sci. 139 (2018) 83-96. https://doi.org/10.1016/j.corsci.2018.04.041.

[3] R. Shi, Z. Wang, L. Qiao, X. Pang, Microstructure evolution of in-situ nanoparticles and its comprehensive effect on high strength steel, J. Mater. Sci. Technol. 35 (2019) 1940-1950. https://doi.org/10.1016/j.jmst.2019.05.009.

[4] J. Sanchez, S.F. Lee, M.A. Martin-Rengel, J. Fullea, C. Andrade, J. Ruiz-Hervias, Measurement of hydrogen and embrittlement of high strength steels, Eng. Fail. Anal. 59 (2016) 467-477. https://doi.org/10.1016/j.engfailanal.2015.11.001.

[5] A. Kuduzović, M.C. Poletti, C. Sommitsch, M. Domankova, S. Mitsche, R. Kienreich, Investigations into the delayed fracture susceptibility of 34CrNiMo6 steel, and the opportunities for its application in ultra-high-strength bolts and fasteners, Mater. Sci. Eng. A 590 (2014) 66-73. https://doi.org/10.1016/j.msea.2013.10.019.

[6] R.A. Oriani, P.H. Josephic, Equilibrium and kinetic studies of the hydrogen-assisted cracking of steel, Acta Metall. 25 (1977) 979-988. https://doi.org/10.1016/0001-6160(77)90126-2.

[7] S. Wang, M.L. Martin, P. Sofronis, S. Ohnuki, N. Hashimoto, I.M. Robertson, Hydrogen-induced intergranular failure of iron, Acta Mater. 69 (2014) 275-282. https://doi.org/10.1016/j.actamat.2014.01.060.

[8] Y.S. Chen, H. Lu, J. Liang, A. Rosenthal, H. Liu, G. Sneddon, I. McCarroll, Z. Zhao, W. Li, A. Guo, J.M. Cairney, Observation of hydrogen trapping at dislocations, grain boundaries, and precipitates, Science 367 (2020) 171-175. https://doi.org/10.1126/ science.aaz0122.

[9] M.L. Martin, M. Dadfarnia, A. Nagao, S. Wang, P. Sofronis, Enumeration of the hydrogen-enhanced localized plasticity mechanism for hydrogen embrittlement in structural materials, Acta Mater. 165 (2019) 734-750. https://doi.org/10.1016/j.actamat. 2018.12.014.

[10] S. Frappart, A. Oudriss, X. Feaugas, J. Creus, J. Bouhattate, F. Thebault, L. Delattre, H. Marchebois, Hydrogen trapping in martensitic steel investigated using electrochemical permeation and thermal desorption spectroscopy, Scr. Mater. 65 (2011) 859-862. https://doi.org/10.1016/j.scriptamat.2011.07.042.

[11] D. Guedes, L. Cupertino Malheiros, A. Oudriss, S. Cohendoz, J. Bouhattate, J. Creus, F. Thébault, M. Piette, X. Feaugas, The role of plasticity and hydrogen flux in the fracture of a tempered martensitic steel: A new design of mechanical test until fracture to separate the influence of mobile from deeply trapped hydrogen, Acta Mater. 186 (2020) 133-148. https://doi.org/10.1016/j.actamat.2019.12.045.

[12] P. Novak, R. Yuan, B.P. Somerday, P. Sofronis, R.O. Ritchie, A statistical, physical-based, micro-mechanical model of hydrogen-induced intergranular fracture in steel, J. Mech. Phys. Solids 58 (2010) 206-226. https://doi.org/10.1016/j.jmps.2009.10.005.

[13] L. Chen, X. Xiong, X. Tao, Y. Su, L. Qiao, Effect of dislocation cell walls on hydrogen adsorption, hydrogen trapping and hydrogen embrittlement resistance, Corros. Sci. 166 (2020). https://doi.org/10.1016/j.corsci.2020.108428.

[14] H. Dogan, D. Li, J.R. Scully, Controlling hydrogen embrittlement in precharged ultrahigh-strength steels, Corrosion 63 (2007) 689-703. https://doi.org/10.5006/ 1.3278418.

[15] W. Krieger, S.V. Merzlikin, A. Bashir, A. Szczepaniak, H. Springer, M. Rohwerder, Spatially resolved localization and characterization of trapped hydrogen in zero to three dimensional defects inside ferritic steel, Acta Mater. 144 (2018)

235-244. https://doi.org/10.1016/j.actamat.2017.10.066.

[16] A. Drexler, T. Depover, S. Leitner, K. Verbeken, W. Ecker, Microstructural based hydrogen diffusion and trapping models applied to Fe–C–X alloys, J. Alloys Compd. 826 (2020) 154057. https://doi.org/10.1016/j.jallcom.2020.154057.

[17] A. Nagao, M. Dadfarnia, B.P. Somerday, P. Sofronis, R.O. Ritchie, Hydrogen-enhanced-plasticity mediated decohesion for hydrogen-induced intergranular and "quasi-cleavage" fracture of lath martensitic steels, J. Mech. Phys. Solids 112 (2018) 403-430. https://doi.org/10.1016/j.jmps.2017.12.016.

[18] T. Depover, K. Verbeken, The effect of TiC on the hydrogen induced ductility loss and trapping behavior of Fe-C-Ti alloys, Corros. Sci. 112 (2016) 308-326. https://doi.org/10.1016/j.corsci.2016.07.013.

[19] M.A. Mohtadi-Bonab, J.A. Szpunar, L. Collins, R. Stankievech, Evaluation of hydrogen induced cracking behavior of API X70 pipeline steel at different heat treatments, Int. J. Hydrogen Energy 39 (2014) 6076-6088. https://doi.org/10.1016/j.ijhydene.2014.01.138.

[20] J. Venezuela, Q. Zhou, Q. Liu, M. Zhang, A. Atrens, Hydrogen Trapping in Some Automotive Martensitic Advanced High-Strength Steels, Adv. Eng. Mater. 20 (2018) 1700468. https://doi.org/10.1002/adem.201700468.

[21] Q. Liu, J. Venezuela, M. Zhang, Q. Zhou, A. Atrens, Hydrogen trapping in some advanced high strength steels, Corros. Sci. 111 (2016) 770-785. https://doi.org/10.1016/j.corsci.2016.05.046.

[22] H.B. Xue, Y.F. Cheng, Characterization of inclusions of X80 pipeline steel and its correlation with hydrogen-induced cracking, Corros. Sci. 53 (2011) 1201-1208. https://doi.org/10.1016/j.corsci.2010.12.011.

[23] S.K. Yen, I.B. Huang, Critical hydrogen concentration for hydrogen-induced blistering on AISI 430 stainless steel, Mater. Chem. Phys. 80 (2003) 662-666. https://doi.org/10.1016/s0254-0584(03)00084-1.

[24] M.A. Mohtadi-Bonab, J.A. Szpunar, S.S. Razavi-Tousi, Hydrogen induced cracking susceptibility in different layers of a hot rolled X70 pipeline steel, Int. J. Hydrogen Energy 38 (2013) 13831-13841. https://doi.org/10.1016/j.ijhydene.

2013.08.046.

[25] Y. Snir, S. Haroush, A. Dannon, A. Landau, D. Eliezer, Y. Gelbstein, Aging condition and trapped hydrogen effects on the mechanical behavior of a precipitation hardened martensitic stainless steel, J. Alloys Compd. 805 (2019) 509-516. https://doi.org/10.1016/j.jallcom.2019.07.112.

[26] J. Venezuela, F.Y. Lim, L. Liu, S. James, Q. Zhou, R. Knibbe, M. Zhang, H. Li, F. Dong, M.S. Dargusch, A. Atrens, Hydrogen embrittlement of an automotive 1700 MPa martensitic advanced high-strength steel, Corros. Sci. 171 (2020) 108726. https://doi.org/10.1016/j.corsci.2020.108726.

[27] J. Venezuela, C. Tapia-Bastidas, Q. Zhou, T. Depover, K. Verbeken, E. Gray, Q. Liu, Q. Liu, M. Zhang, A. Atrens, Determination of the equivalent hydrogen fugacity during electrochemical charging of 3.5NiCrMoV steel, Corros. Sci. 132 (2018) 90-106. https://doi.org/10.1016/j.corsci.2017.12.018.

[28] J. Venezuela, J. Blanch, A. Zulkiply, Q. Liu, Q. Zhou, M. Zhang, A. Atrens, Further study of the hydrogen embrittlement of martensitic advanced high-strength steel in simulated auto service conditions, Corros. Sci. 135 (2018) 120-135. https://doi.org/10.1016/j.corsci.2018.02.037.

[29] E.I. Galindo-Nava, B.I.Y. Basha, P.E.J. Rivera-Díaz-del-Castillo, Hydrogen transport in metals: Integration of permeation, thermal desorption and degassing, J. Mater. Sci. Technol. 33 (2017) 1433-1447. https://doi.org/10.1016/j.jmst.2017.09.011.

[30] T. Schaffner, A. Hartmaier, V. Kokotin, M. Pohl, Analysis of hydrogen diffusion and trapping in ultra-high strength steel grades, J. Alloys Compd. 746 (2018) 557-566. https://doi.org/10.1016/j.jallcom.2018.02.264.

[31] M.A.V. Devanathan, Z. Stachurski, The Mechanism of Hydrogen Evolution on Iron in Acid Solutions by Determination of Permeation Rates, J. Electrochem. Soc. 111 (1964) 619-623. https://doi.org/10.1149/1.2426195.

[32] T.Y. Zhang, Y.P. Zheng, Effects of absorption and desorption on hydrogen permeation—I. Theoretical modeling and room temperature verification, Acta Mater. 46 (1998) 5023-5033. https://doi.org/10.1016/s1359-6454(98)00176-1.

[33] Q. Liu, A.D. Atrens, Z. Shi, K. Verbeken, A. Atrens, Determination of the

hydrogen fugacity during electrolytic charging of steel, Corros. Sci. 87 (2014) 239-258. https://doi.org/10.1016/j.corsci.2014.06.033.

[34] J.-Y. Lee, S.M. Lee, Hydrogen trapping phenomena in metals with B.C.C. and F.C.C. crystals structures by the desorption thermal analysis technique, Surf. Coat. Technol. 28 (1986) 301-314. https://doi.org/10.1016/0257-8972(86)90087-3.

[35] G.M. Pressouyre, A classification of hydrogen traps in steel, Metall. Trans. A 10 (1979) 1571-1573. https://doi.org/10.1007/bf02812023.

[36] R.M. Barrer, Diffusion in and through solids, second ed., Cambridge University Press, London, 1951.

[37] D. Pérez Escobar, T. Depover, E. Wallaert, L. Duprez, M. Verhaege, K. Verbeken, Thermal desorption spectroscopy study of the interaction between hydrogen and different microstructural constituents in lab cast Fe–C alloys, Corros. Sci. 65 (2012) 199-208. https://doi.org/10.1016/j.corsci.2012.08.017.

[38] J. Venezuela, E. Gray, Q. Liu, Q. Zhou, C. Tapia-Bastidas, M. Zhang, A. Atrens, Equivalent hydrogen fugacity during electrochemical charging of some martensitic advanced high-strength steels, Corros. Sci. 127 (2017) 45-58. https://doi.org/10.1016/j.corsci.2017.08.011.

[39] E. Wallaert, T. Depover, M. Arafin, K. Verbeken, Thermal desorption spectroscopy evaluation of the hydrogen-trapping capacity of NbC and NbN precipitates, Metall. Mater. Trans. A 45 (2014) 2412-2420. https://doi.org/10.1007/s11661-013-2181-1.

[40] T. Bastidas, C. Vladimir, The Design, Construction and Implementation of a Novel State-of-the-Art Thermal Desorption Spectrometer for the Study of Hydrogen Embrittlement of Medium Strength Steels, Griffith University, 2016.

[41] F.G. Wei, K. Tsuzaki, Quantitative analysis on hydrogen trapping of TiC particles in steel, Metall. Mater. Trans. A 37 (2006) 331-353. https://doi.org/10.1007/s11661-006-0004-3.

[42] H. Asahi, D. Hirakami, S. Yamasaki, Hydrogen trapping behavior in vanadium-added steel, ISIJ Int. 43 (2003) 527-533. https://doi.org/10.2355/isijinternational. 43.527.

[43] X. Jin, L. Xu, W. Yu, K. Yao, J. Shi, M. Wang, The effect of undissolved and temper-induced (Ti,Mo)C precipitates on hydrogen embrittlement of quenched and tempered Cr-Mo steel, Corros. Sci. 166 (2020) 108421. https://doi.org/10.1016/j.corsci.2019.108421.

[44] R. Silverstein, D. Eliezer, E. Tal-Gutelmacher, Hydrogen trapping in alloys studied by thermal desorption spectrometry, J. Alloys Compd. 747 (2018) 511-522. https://doi.org/10.1016/j.jallcom.2018.03.066.

[45] A. Drexler, T. Depover, K. Verbeken, W. Ecker, Model-based interpretation of thermal desorption spectra of Fe-C-Ti alloys, J. Alloys Compd. 789 (2019) 647-657. https://doi.org/10.1016/j.jallcom.2019.03.102.

[46] F.G. Wei, T. Hara, K. Tsuzaki, Precise determination of the activation energy for desorption of hydrogen in two Ti-added steels by a single thermal-desorption spectrum, Metall. Mater. Trans. B 35 (2004) 587-597. https://doi.org/10.1007/s11663-004-0057-x.

[47] M. Itakura, H. Kaburaki, M. Yamaguchi, T. Okita, The effect of hydrogen atoms on the screw dislocation mobility in bcc iron: A first-principles study, Acta Mater. 61 (2013) 6857-6867. https://doi.org/10.1016/j.actamat.2013.07.064.

[48] G.K. Williamson, W.H. Hall, X-ray line broadening from filed aluminium and wolfram, Acta Metall. 1 (1953) 22-31. https://doi.org/10.1016/0001-6160(53)90006-6.

[49] S. Takebayashi, T. Kunieda, N. Yoshinaga, K. Ushioda, S. Ogata, Comparison of the dislocation density in martensitic steels evaluated by some X-ray diffraction methods, ISIJ Int. 50 (2010) 875-882. https://doi.org/10.2355/isijinternational.50.875.

[50] J.P. Hirth, Effects of hydrogen on the properties of iron and steel, Metall. Trans. A 11 (1980) 861-890. https://doi.org/10.1007/bf02654700.

[51] C. Zhou, B. Ye, Y. Song, T. Cui, P. Xu, L. Zhang, Effects of internal hydrogen and surface-absorbed hydrogen on the hydrogen embrittlement of X80 pipeline steel, Int. J. Hydrogen Energy 44 (2019) 22547-22558. https://doi.org/10.1016/j.ijhydene.2019.04.239.

[52] T. Depover, K. Verbeken, The detrimental effect of hydrogen at dislocations on the hydrogen embrittlement susceptibility of Fe-C-X alloys: An experimental proof of

the HELP mechanism, Int. J. Hydrogen Energy 43 (2018) 3050-3061. https://doi.org/10. 1016/j.ijhydene.2017.12.109.

[53] C.D. Beachem, A new model for hydrogen-assisted cracking (hydrogen "embrittlement"), Metall. Mater. Trans. B 3 (1972) 441-455. https://doi.org/10.1007/bf02642048.

[54] S.P. Lynch, Environmentally assisted cracking: Overview of evidence for an adsorption-induced localised-slip process, Acta Metall. 36 (1988) 2639-2661. https://doi.org/10.1016/0001-6160(88)90113-7.

[55] A. Turk, D. San Martin, P.E.J. Rivera-Diaz-del-Castillo, E.I. Galindo-Nava, Correlation between vanadium carbide size and hydrogen trapping in ferritic steel, Scr. Mater. 152 (2018) 112-116. https://doi.org/10.1016/j.scriptamat.2018.04.013.

[56] J. Takahashi, K. Kawakami, Y. Kobayashi, T. Tarui, The first direct observation of hydrogen trapping sites in TiC precipitation-hardening steel through atom probe tomography, Scr. Mater. 63 (2010) 261-264. https://doi.org/10.1016/j.scriptamat. 2010.03.012.

[57] D. Di Stefano, R. Nazarov, T. Hickel, J. Neugebauer, M. Mrovec, C. Elsässer, First-principles investigation of hydrogen interaction with TiC precipitates in α-Fe, Phys. Rev. B 93 (2016) 184108. https://doi.org/10.1103/PhysRevB.93.184108.

[58] J. Li, X. Gao, L. Du, Z. Liu, Relationship between microstructure and hydrogen induced cracking behavior in a low alloy pipeline steel, J. Mater. Sci. Technol. 33 (2017) 1504-1512. https://doi.org/10.1016/j.jmst.2017.09.013.

[59] J. Takahashi, K. Kawakami, Y. Kobayashi, Origin of hydrogen trapping site in vanadium carbide precipitation strengthening steel, Acta Mater. 153 (2018) 193-204. https://doi.org/10.1016/j.actamat.2018.05.003.

[60] Y.S. Chen, D. Haley, S.S. Gerstl, A.J. London, F. Sweeney, R.A. Wepf, W.M. Rainforth, P.A. Bagot, M.P. Moody, Direct observation of individual hydrogen atoms at trapping sites in a ferritic steel, Science 355 (2017) 1196-1199. https://doi.org/10.1126/science.aal2418.

[61] B. Malard, B. Remy, C. Scott, A. Deschamps, J. Chêne, T. Dieudonné, M.H. Mathon, Hydrogen trapping by VC precipitates and structural defects in a high

strength Fe–Mn–C steel studied by small-angle neutron scattering, Mater. Sci. Eng. A 536 (2012) 110-116. https://doi.org/10.1016/j.msea.2011.12.080.

[62] F. G. Wei and K. Tsuzaki, "Hydrogen trapping character of nano-sized NbC precipitates in tempered martensite", Effects of Hydrogen on Materials, Proc. 2008 Intl. Hydrogen Conference, B. Somerday et al. edited, ASM Intl., 2009, pp.456-463.

[63] F.G. Wei, T. Hara, K. Tsuzaki, Nano-preciptates design with hydrogen trapping character in high strength steel, in: Proceedings of the 2008 International Hydrogen Conference–Effects of Hydrogen on Materials, 2009, pp. 448–455.

[64] R.G. Baker, J. Nutting, Precipitation processes in steels, Iron and Steel Institute, Special Report, 64 (1959) 1-22.

[65] U. Dahmen, Orientation relationships in precipitation systems, Acta Metall. 30 (1982) 63-73. https://doi.org/10.1016/0001-6160(82)90045-1.

[66] G.M. Pressouyre, I.M. Bernstein, A quantitative analysis of hydrogen trapping, Metall. Trans. A 9(1978) 1571-1580. https://doi.org/10.1007/bf02661939.

[67] A. Nagao, M.L. Martin, M. Dadfarnia, P. Sofronis, I.M. Robertson, The effect of nanosized (Ti,Mo)C precipitates on hydrogen embrittlement of tempered lath martensitic steel, Acta Mater. 74 (2014) 244-254. https://doi.org/10.1016/j.actamat. 2014.04.051.

[68] H.-J. Kim, S.-H. Jeon, W.-S. Yang, B.-G. Yoo, Y.-D. Chung, H.-Y. Ha, H.-Y. Chung, Effects of titanium content on hydrogen embrittlement susceptibility of hot-stamped boron steels, J. Alloys Compd. 735 (2018) 2067-2080. https://doi.org/10.1016/j.jallcom. 2017.12.004.

[69] T. Depover, K. Verbeken, Evaluation of the effect of V_4C_3 precipitates on the hydrogen induced mechanical degradation in Fe-C-V alloys, Mater. Sci. Eng. A 675 (2016) 299-313. https://doi.org/10.1016/j.msea.2016.08.053.

[70] Q. Cui, J. Wu, D. Xie, X. Wu, Y. Huang, X. Li, Effect of Nanosized NbC Precipitates on Hydrogen Diffusion in X80 Pipeline Steel, Materials 10 (2017). https://doi.org/10.3390/ma10070721.

[71] R. Silverstein, B. Glam, D. Eliezer, D. Moreno, S. Eliezer, Dynamic deformation of hydrogen charged austenitic-ferritic steels: Hydrogen trapping mechanisms, and

simulations, J. Alloys Compd. 731 (2018) 1238-1246. https://doi.org/10.1016/j.jallcom. 2017.10.142.

[72] C. Park, N. Kang, S. Liu, Effect of grain size on the resistance to hydrogen embrittlement of API 2W Grade 60 steels using in situ slow-strain-rate testing, Corros. Sci. 128 (2017) 33-41. https://doi.org/10.1016/j.corsci.2017.08.032.

[73] L.W. Tsay, H.L. Lu, C. Chen, The effect of grain size and aging on hydrogen embrittlement of a maraging steel, Corros. Sci. 50 (2008) 2506-2511. https://doi.org/10.1016/j.corsci.2008.06.044.

[74] Y.H. Fan, B. Zhang, J.Q. Wang, E.H. Han, W. Ke, Effect of grain refinement on the hydrogen embrittlement of 304 austenitic stainless steel, J. Mater. Sci. Technol. 35 (2019) 2213-2219. https://doi.org/10.1016/j.jmst.2019.03.043.

[75] Y.H. Fan, F. Cui, L. Lu, B. Zhang, A nanotwinned austenite stainless steel with high hydrogen embrittlement resistance, J. Alloys Compd. 788 (2019) 1066-1075. https://doi.org/10.1016/j.jallcom.2019.02.312.

[76] K.-S. Kim, J.-H. Kang, S.-J. Kim, Effect of Grain Boundary Carbide on Hydrogen Embrittlement in Stable Austenitic Stainless Steels, ISIJ Int. 59 (2019) 1136-1144. https://doi.org/10.2355/isijinternational.ISIJINT-2018-639.

[77] Y.F. Jiang, B. Zhang, Y. Zhou, J.Q. Wang, E.H. Han, W. Ke, Atom probe tomographic observation of hydrogen trapping at carbides/ferrite interfaces for a high strength steel, J. Mater. Sci. Technol. 34 (2018) 1344-1348. https://doi.org/10.1016/j.jmst.2017.11.008.

[78] E.K. Storms, N.H. Krikorian, The Variation of Lattice Parameter with Carbon Content of Niobium Carbide, J. Phys. Chem. 63 (1959) 1747-1749. https://doi.org/10.1021/j150580a042.

[79] S.M. Lee, J.Y. Lee, The effect of the interface character of TiC particles on hydrogen trapping in steel, Acta Metall. 35 (1987) 2695-2700. https://doi.org/10.1016/0001-6160(87)90268-9.

[80] F.-G. Wei, T. Hara, T. Tsuchida, K. Tsuzaki, Hydrogen Trapping in Quenched and Tempered 0.42C-0.30Ti Steel Containing Bimodally Dispersed TiC Particles, ISIJ Int. 43 (2003) 539-547. https://doi.org/10.2355/isijinternational.43.539.

[81] Q. Liu, A. Atrens, Reversible hydrogen trapping in a 3.5NiCrMoV medium strength steel, Corros. Sci. 96 (2015) 112-120. https://doi.org/10.1016/j.corsci. 2015.04.011.

[82] A.J. Haq, K. Muzaka, D.P. Dunne, A. Calka, E.V. Pereloma, Effect of microstructure and composition on hydrogen permeation in X70 pipeline steels, Int. J. Hydrogen Energy 38 (2013) 2544-2556. https://doi.org/10.1016/j.ijhydene. 2012.11.127.

[83] T. Gladman, Precipitation hardening in metals, Mater. Sci. Technol. 15 (2013) 30-36. https://doi.org/10.1179/026708399773002782.

[84] Y. Kobayashi, J. Takahashi, K. Kawakami, Experimental evaluation of the particle size dependence of the dislocation–particle interaction force in TiC-precipitation-strengthened steel, Scr. Mater. 67 (2012) 854-857. https://doi.org/10.1016/j.scriptamat. 2012.08.005.

[85] H.K. Dharamshi, H. Bhadeshia, Prevention of Hydrogen Embrittlement in Steels, ISIJ Int. 56 (2016) 24-36. https://doi.org/10.2355/isijinternational.ISIJINT-2015-430.

Table and Figure captions

Table 1 Summary of the hydrogen permeation parameters and the densities of hydrogen trapping sites in first and second permeation transients.

Table 2 Summary of SADP results for the grain-boundary carbide in Fig. 8

Fig. 1. (a) X-ray diffraction pattern of the investigated quenched and tempered steel. (b) Representative SEM micrograph of the microstructure. The major phase in the sample is bcc tempered martensite. (c) The morphology and distribution of tempered lath martensite and grain boundaries; the details are indicated in the enlarged inset.

Fig. 2. Electrochemical hydrogen permeation curves for the (a) first and (b) second permeation in the investigated steel.

Fig. 3. (a) The relationship between hydrogen charging time and the hydrogen concentration at the mid-plane of the plate. (b) Hydrogen desorption rate curve of the investigated steel.

Fig. 4. (a) TEM bright-field image showing the microstructure of the martensite lath distribution; (b) corresponding dark-field image of (a). (c) TEM image showing dislocations with high density. (d) The interaction between nanoprecipitates and dislocations.

Fig. 5. Measurement and analysis of the dislocation density for the investigated steel by XRD: (a), (b), (c), (d), and (e) are XRD peaks corresponding to the (110), (200), (211), (220), and (310) planes, respectively; (f) Williamson–Hall plots for the diffraction patterns of the investigated steel.

Fig. 6. TEM micrographs showing the overall microstructure of NbC distribution. (a) TEM image showing the microstructure and distribution of the precipitates. (b) The corresponding enlarged view of the dotted box in (a). (c) bright-field micrograph and the corresponding selected-area diffraction pattern (SADP) in the inset, (d) the corresponding dark-field image. (e) The size distribution of the NbC nanoprecipitates.

Fig. 7. HRTEM observation of one NbC with the dimeter of 12 nm. (a) HRTEM image of the NbC with the surrounding martensite matrix. (b1) FFT, (b2) IFFT of the

selected yellow box in (a) indicating the fcc NbC along $[1\bar{1}0]_{NbC}$. (b3) FFT, (b4) IFFT of the selected red box in (a) indicating the bcc α-Fe matrix along $[001]_{\alpha\text{-Fe}}$. (c) The corresponding FFT patterns of the NbC with the surrounding matrix. (d) The IFFT of the NbC and the surrounding matrix in white box of (a). (e) The enlarged image in dashed rectangle in (d) showing the interfacial structures for the NbC/α-Fe interface. (d) Schematic summarizing of the diffraction spots, showing no obvious OR.

Fig. 8. (a) TEM bright-field micrograph showing the presence of a grain boundary with grain-boundary precipitates. (b) Morphology of a typical grain-boundary carbide. (c) SADP of the area shown by the white dashed circle in (b). (d) Schematic of the diffraction spots from (c). (e) The corresponding EDS spectra and the element contents shown by the white dashed circle in (b).

Fig. 9. (a-b) TEM images in the as-quenched specimen in this work. (c) The corresponding EDS spectra and the element contents shown by the red dashed circle in (b).

Fig. 10. Schematic of the hydrogen trapping of different microstructures in tempered martensitic steel.

Tables

Table 1 Summary of the hydrogen permeation parameters and the densities of hydrogen trapping sites in first and second permeation transients.

Permeation	I_∞/A, **μA/cm²**	$t_{0.63}$, **s**	D_{eff}, 10^{-6} **cm²/s**	C_{ap}, 10^{-5} **mol/cm³**	N_t, 10^{20} **cm⁻³**
First (reversible and irreversible H)	27.5	1467	1.63	2.09	3.24
Second (reversible H)	27.2	1230	1.95	1.73	2.24

Table 2 Summary of SADP results for the grain-boundary carbide in Fig. 8

Matrix/ Precipitation	**α-Fe-bcc-1 *Z* = [011]**			**α-Fe-bcc-2 *Z* = [111]**			**NbC-fcc *Z* = [011]**		
Spot	1	2	3	4	5	6	7	8	9
Lattice plane	$(0\bar{1}1)$	$(\bar{2}\bar{1}1)$	$(\bar{2}00)$	$(10\bar{1})$	$(01\bar{1})$	$(\bar{1}10)$	$(11\bar{1})$	(200)	$(1\bar{1}1)$
Spacing (SADP), Å	2.033	1.176	1.441	2.039	2.030	2.040	2.607	2.346	2.660
Spacing (Calc), Å	2.027	1.170	1.433	2.027	2.027	2.027	2.581	2.235	2.581
Angle (SADP), deg.	54.9		35.4	59.9		60.3	54.2		55.4
Angle (Calc), deg.	54.7		35.3	60.0		60.0	54.7		54.7

Figures

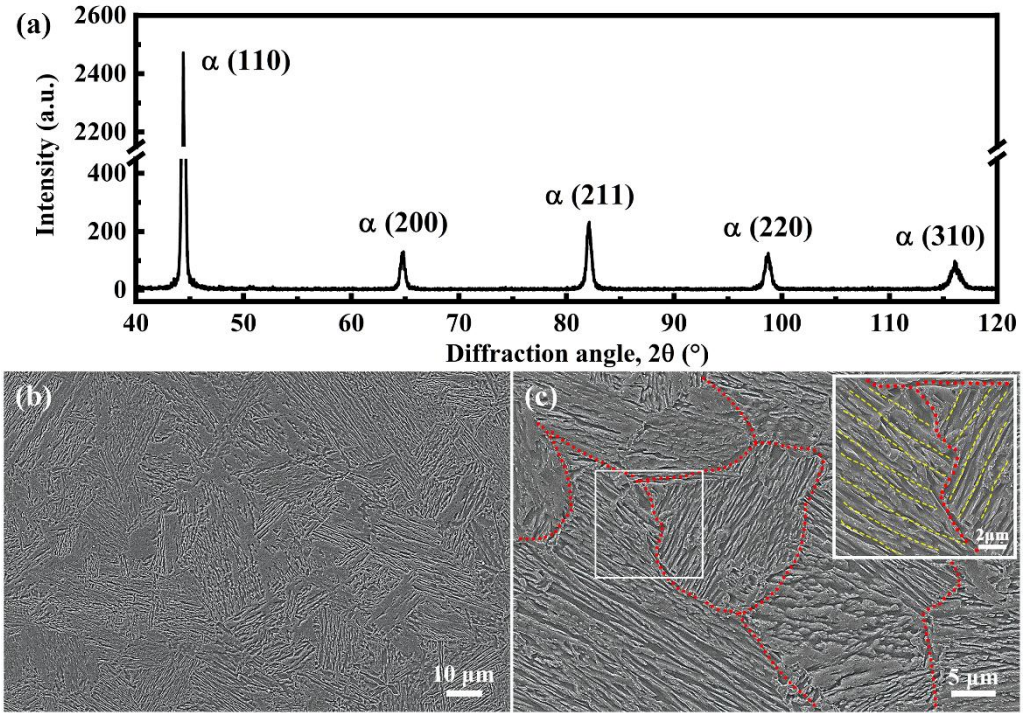

Fig. 1. (a) X-ray diffraction pattern of the investigated quenched and tempered steel. (b) Representative SEM micrograph of the microstructure. The major phase in the sample is bcc tempered martensite. (c) The morphology and distribution of tempered lath martensite and grain boundaries; the details are indicated in the enlarged inset.

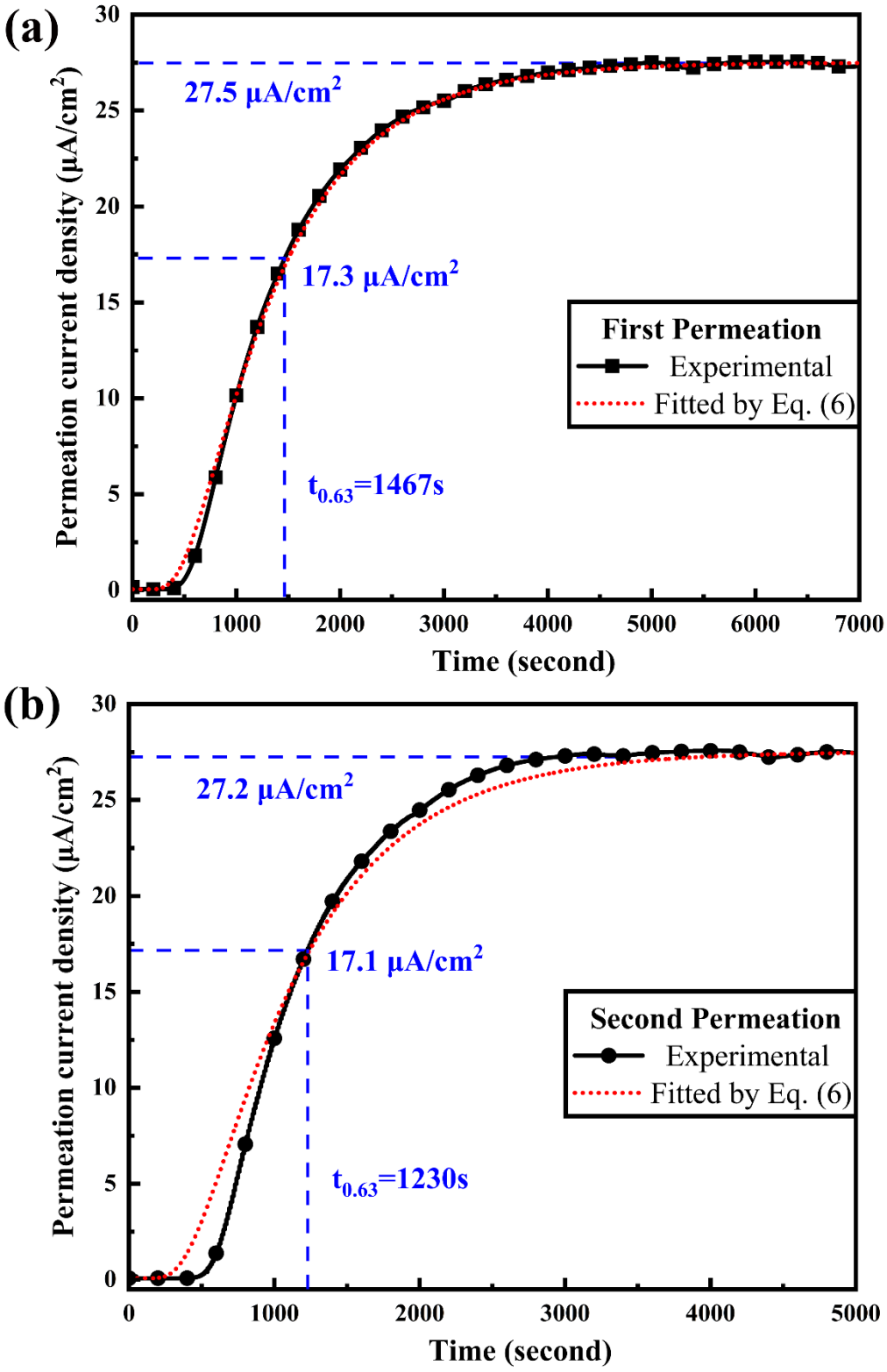

Fig. 2. Electrochemical hydrogen permeation curves for the (a) first and (b) second permeation in the investigated steel.

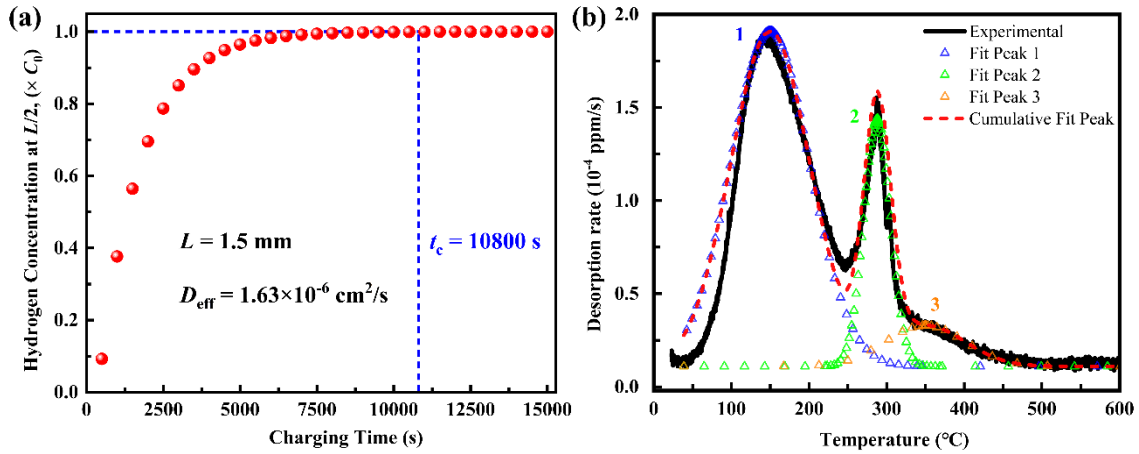

Fig. 3. (a) The relationship between hydrogen charging time and the hydrogen concentration at the mid-plane of the plate. (b) Hydrogen desorption rate curve of the investigated steel.

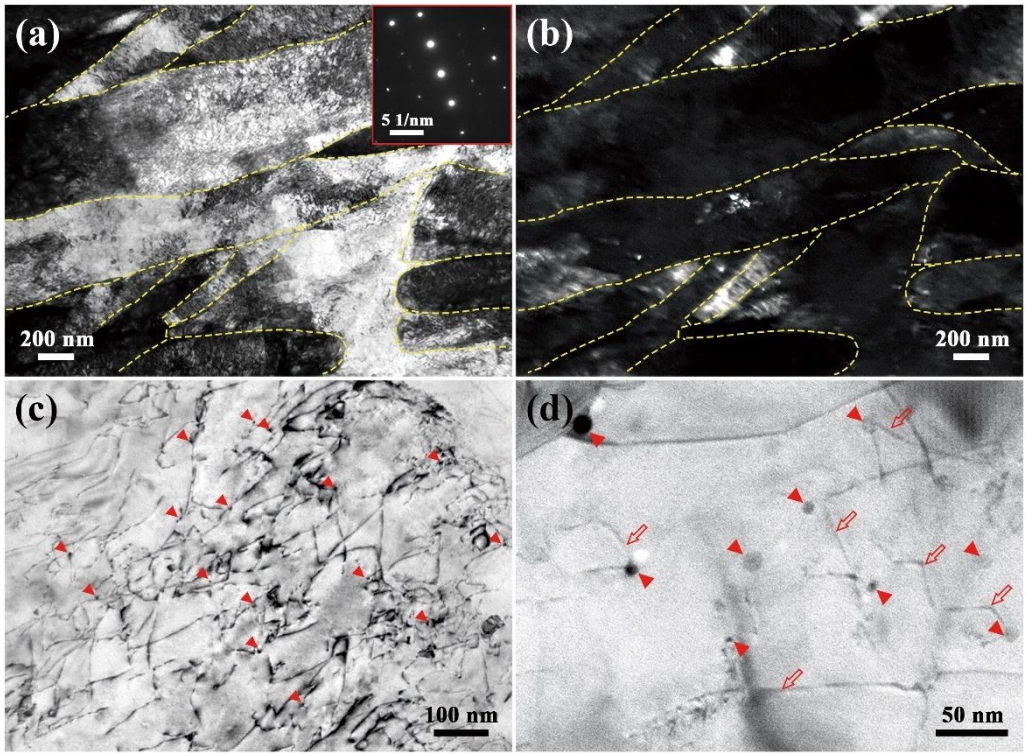

Fig. 4. (a) TEM bright-field image showing the microstructure of the martensite lath distribution; (b) corresponding dark-field image of (a). (c) TEM image showing dislocations with high density. (d) The interaction between nanoprecipitates and dislocations.

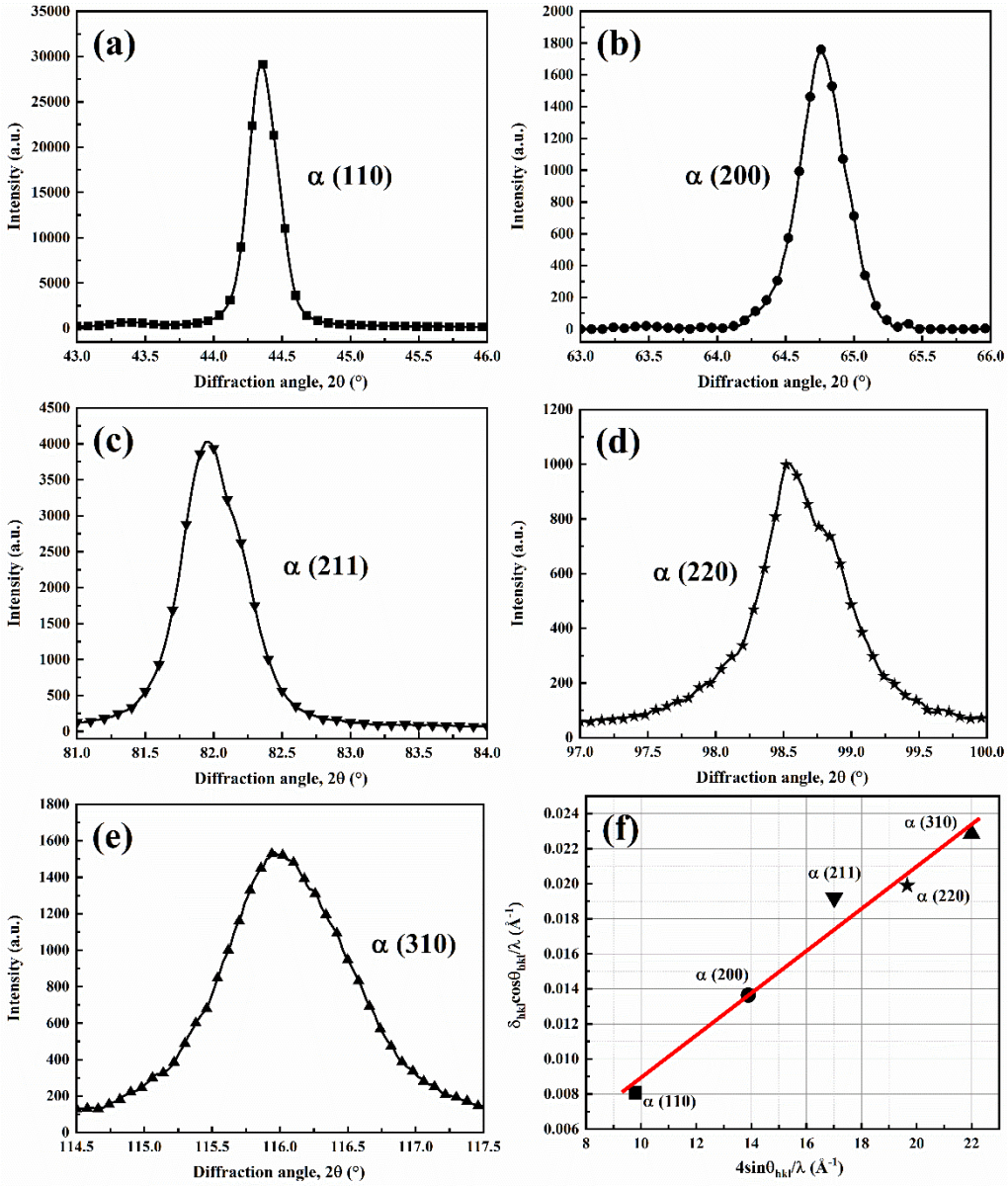

Fig. 5. Measurement and analysis of the dislocation density for the investigated steel by XRD: (a), (b), (c), (d), and (e) are XRD peaks corresponding to the (110), (200), (211), (220), and (310) planes, respectively; (f) Williamson–Hall plots for the diffraction patterns of the investigated steel.

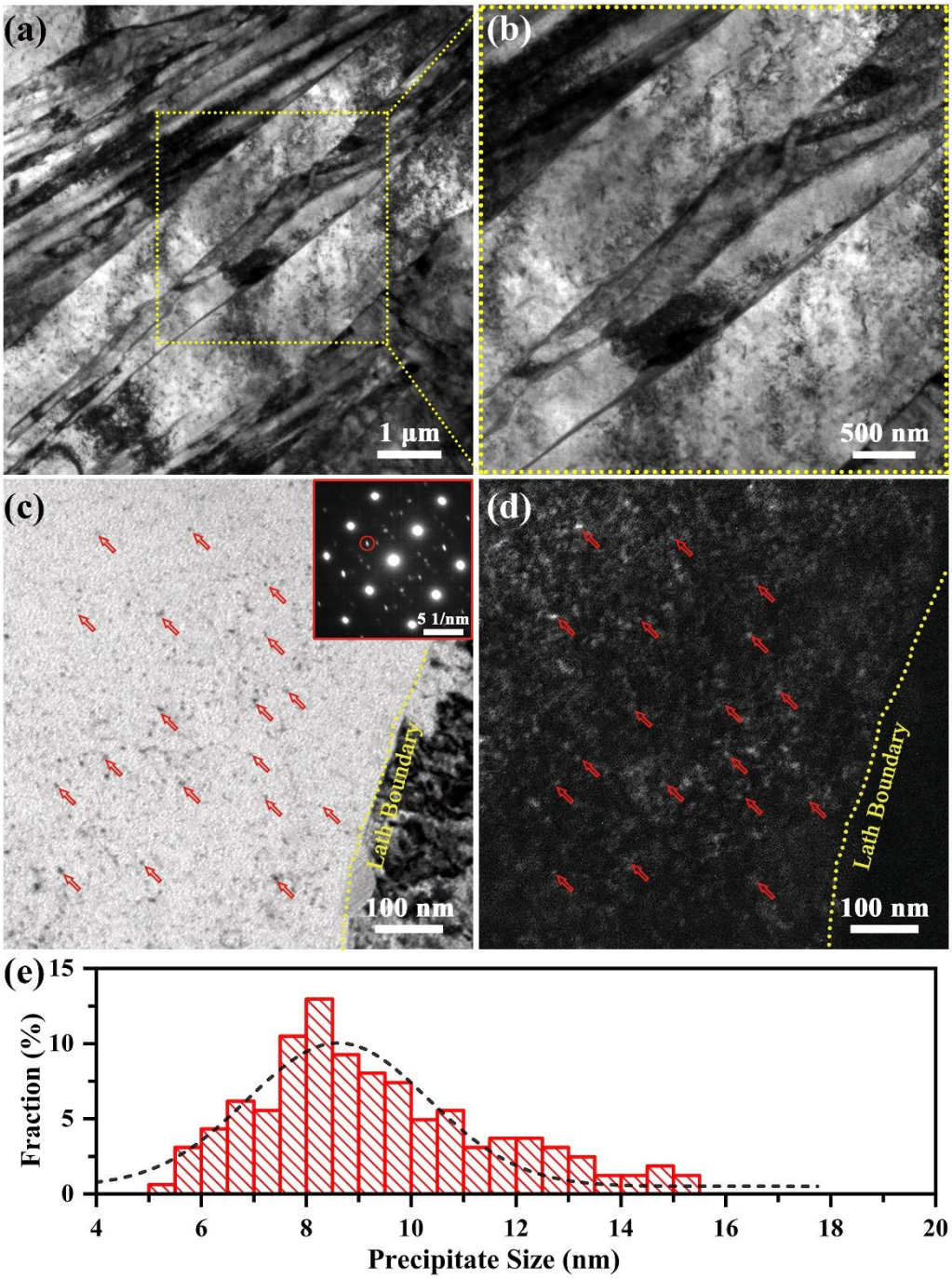

Fig. 6. TEM micrographs showing the overall microstructure of NbC distribution. (a) TEM image showing the microstructure and distribution of the precipitates. (b) The corresponding enlarged view of the dotted box in (a). (c) bright-field micrograph and the corresponding selected-area diffraction pattern (SADP) in the inset, (d) the corresponding dark-field image. (e) The size distribution of the NbC nanoprecipitates.

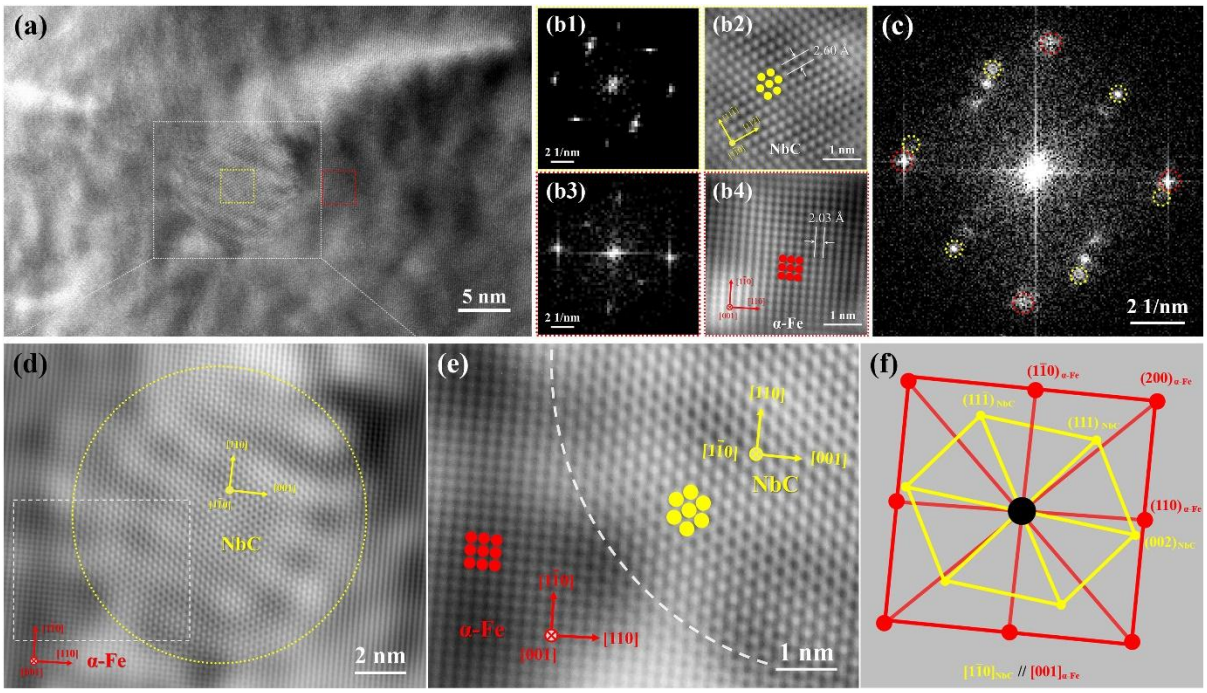

Fig. 7. HRTEM observation of one NbC with the dimeter of 12 nm. (a) HRTEM image of the NbC with the surrounding martensite matrix. (b1) FFT, (b2) IFFT of the selected yellow box in (a) indicating the fcc NbC along $[1\,1\,0]_{NbC}$. (b3) FFT, (b4) IFFT of the selected red box in (a) indicating the bcc α-Fe matrix along $[001]_{\alpha\text{-Fe}}$. (c) The corresponding FFT patterns of the NbC with the surrounding matrix. (d) The IFFT of the NbC and the surrounding matrix in white box of (a). (e) The enlarged image in dashed rectangle in (d) showing the interfacial structures for the NbC/α-Fe interface. (d) Schematic summarizing of the diffraction spots, showing no obvious OR.

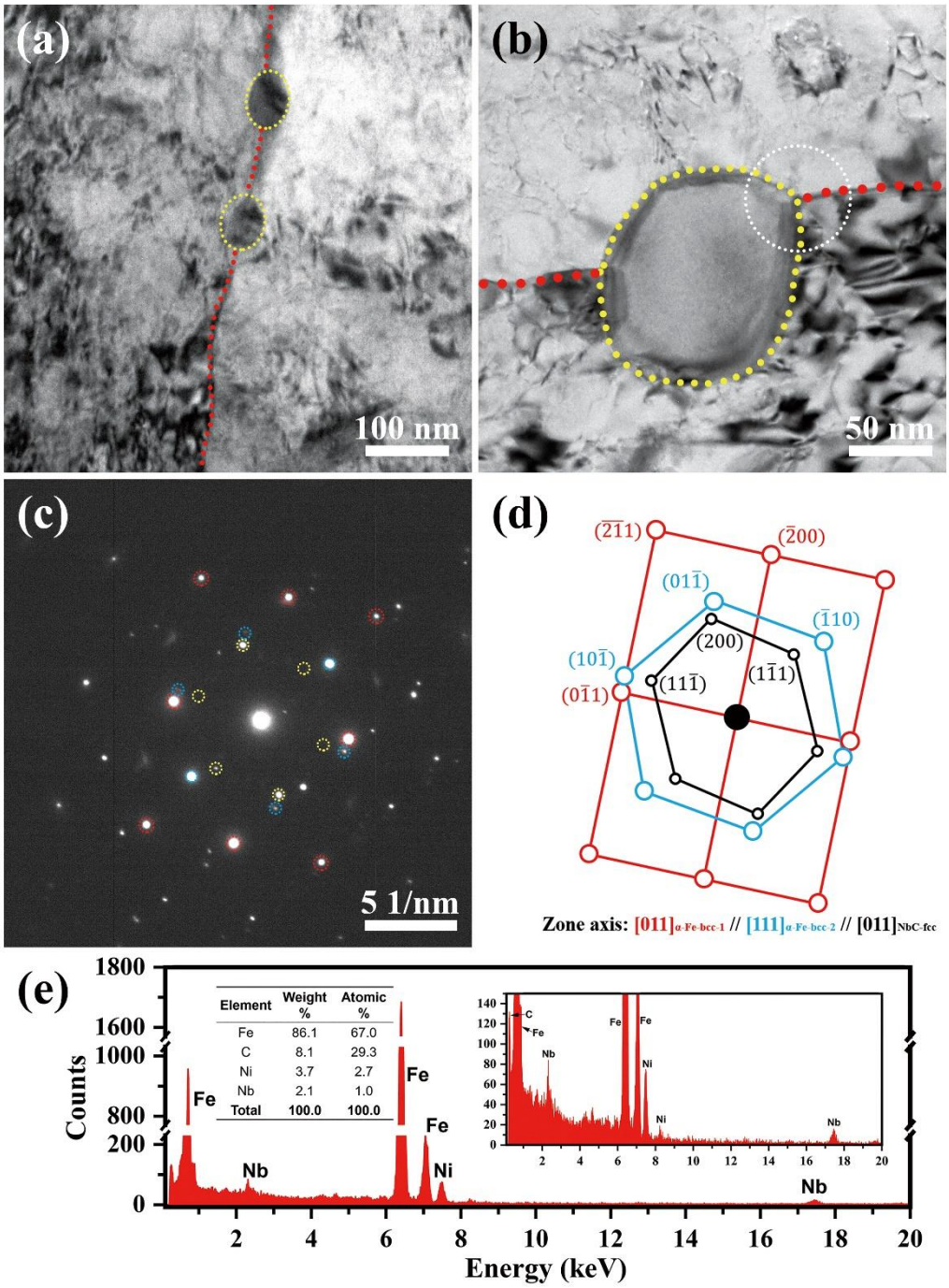

Fig. 8. (a) TEM bright-field micrograph showing the presence of a grain boundary with grain-boundary precipitates. (b) Morphology of a typical grain-boundary carbide. (c) SADP of the area shown by the white dashed circle in (b). (d) Schematic of the diffraction spots from (c). (e) The corresponding EDS spectra and the element contents shown by the white dashed circle in (b).

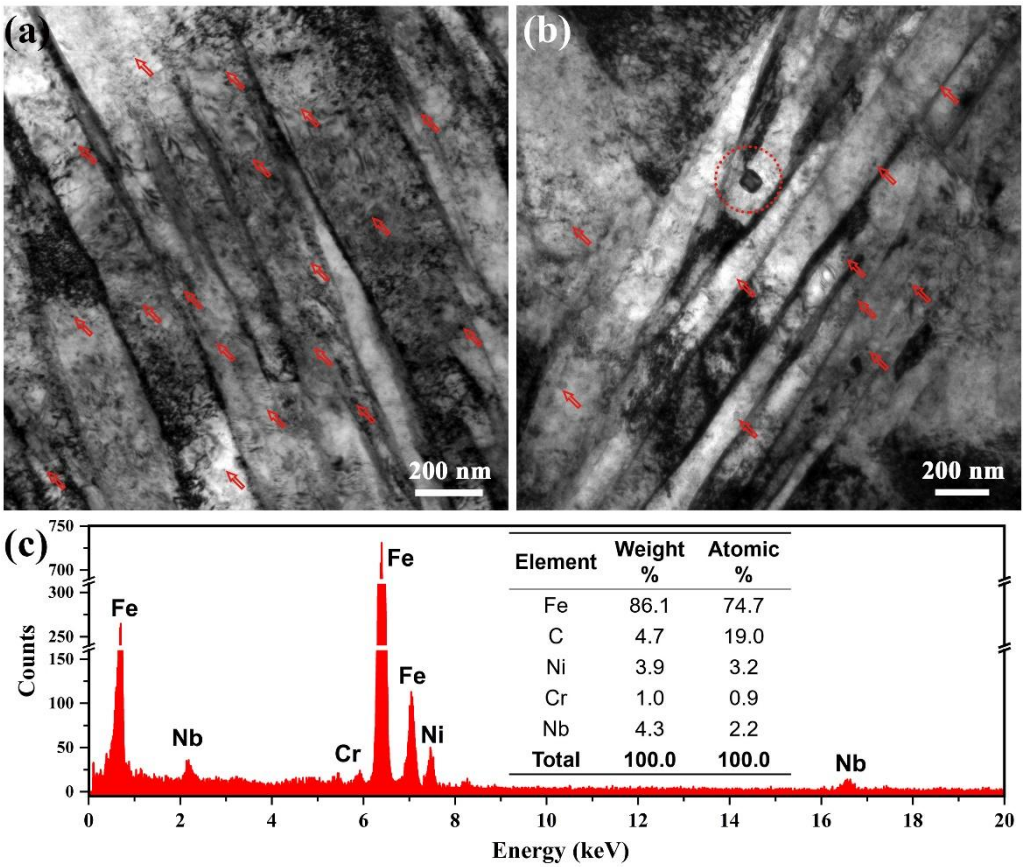

Fig. 9. (a-b) TEM images in the as-quenched specimen in this work. (c) The corresponding EDS spectra and the element contents shown by the red dashed circle in (b).

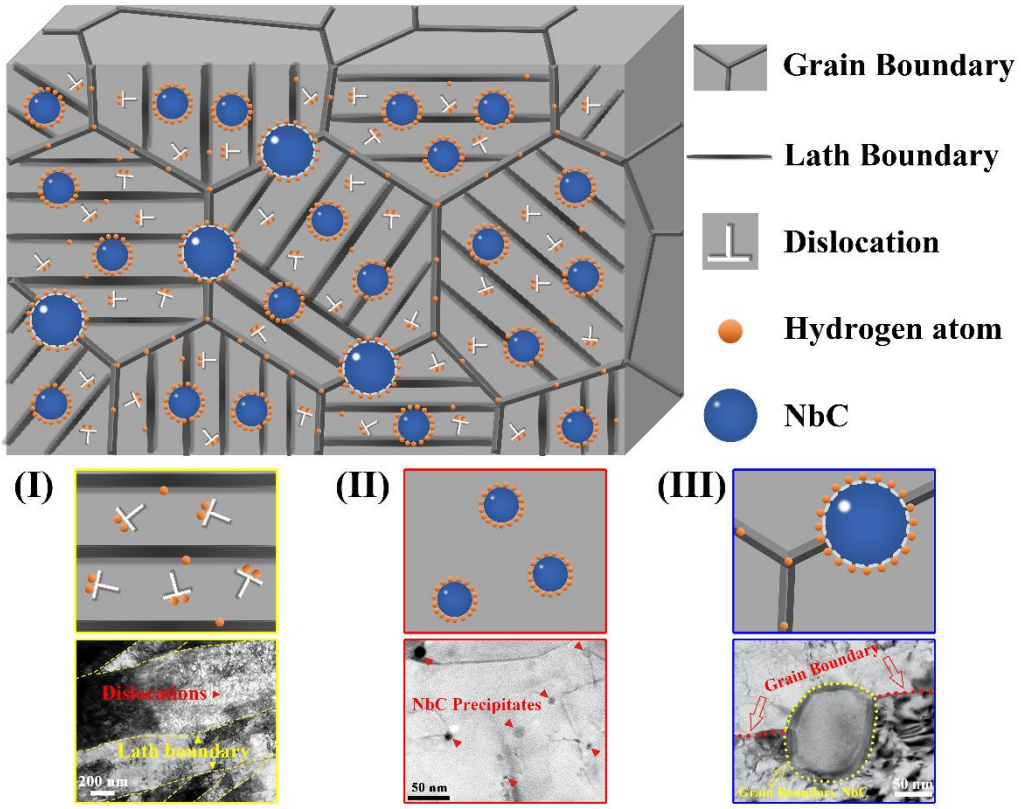

Fig. 10. Schematic of the hydrogen trapping of different microstructures in tempered martensitic steel.